

Suzaku Observation of the Metallicity in the Interstellar Medium of NGC 4258

Saori KONAMI,^{1,2} Kosuke SATO,³ Kyoko MATSUSHITA,¹ Shin'ya YAMADA,⁴ Naoki ISOBE,^{5,2}
Atsushi SENDA,^{6,2} Asami HAYATO,^{1,2} Poshak GANDHI,² Toru TAMAGAWA,^{2,1} and Kazuo MAKISHIMA,^{4,2}

¹ Department of Physics, Tokyo University of Science, 1-3 Kagurazaka, Shinjuku-ku, Tokyo 162-8601

² Cosmic Radiation Laboratory, the Institute of Physical and Chemical Research, 2-1 Hirosawa, Wako, Saitama 351-0198
konami@crab.riken.jp

³ Graduate School of Natural Science and Technology, Kanazawa University, Kakuma, Kanazawa, Ishikawa 920-1192

⁴ Department of Physics, University of Tokyo, 7-3-1, Hongo, Bunkyo-ku, Tokyo, 113-0033

⁵ Department of Astronomy, Kyoto University, Kitashirakawa-Oiwake-cho, Sakyo-ku, Kyoto, 606-8502

⁶ Japan Science and Technology Agency, Kawaguchi Center Building, 4-1-8, Honcho, Kawaguchi-shi, Saitama 332-0012

(Received ; accepted)

Abstract

The Suzaku X-ray satellite observed the nearby spiral galaxy NGC 4258 for a total good exposure time of 100 ks. We present an analysis of the Suzaku XIS data, in which we confirm that the 0.5–2 keV spectra of the interstellar medium (ISM) are well-represented by a two-temperature model. The cool and hot ISM temperatures are $0.23^{+0.01}_{-0.02}$ and 0.59 ± 0.01 keV, respectively. Suzaku's excellent spectral sensitivity enables us to measure the metal abundances of O, Ne, Mg, Si and Fe of the ISM for the first time. The resultant abundance pattern of O, Mg, Si, and Fe is consistent with that of the new solar abundance table of Lodders (2003), rather than Anders & Grevesse (1989). This suggests that the metal enrichment processes of NGC 4258 and of our Galaxy are similar.

Key words: galaxies: individual (NGC 4258), galaxies: interstellar medium, galaxies: abundances

1. Introduction

Metal abundances in the hot X-ray emitting interstellar medium (ISM) are important for understanding the star formation history and evolution of galaxies. A large fraction of metals in the ISM are synthesized by type Ia and type II supernovae (SNe Ia/II). O and Mg are predominantly synthesized by SNe II, while Fe is mainly produced by SNe Ia. Therefore, the abundance ratios provide useful information on the contribution of both types of SNe enriching the metals.

Compared to starburst galaxies, normal spiral galaxies have lower star formation rates (SFRs), and have lower X-ray surface brightness, because the integrated soft X-ray luminosities of spiral galaxies correlate with SFR (Tüllmann et al. 2006). In addition, these galaxies sometimes exhibit strong X-ray emission from the central active galactic nuclei. As a result, it has remained rather difficult to constrain the abundances of their hot ISM over a wide range of species from O to Fe.

In order to determine the metal abundances of O, Ne, S, and Ar from the emission lines in H II regions, several optical observations have been performed (e.g., Pérez-Montero et al. 2007, Crockett et al. 2006). In particular, O emission lines, a good tracer of SNe II, are the brightest in the optical band. However, determination of the metal abundances, including O, has large uncertainty due to dust grains, the composition of which is difficult to ascertain. In addition, no significant Fe lines, a good tracer of SN Ia, exist in the optical band.

The Einstein satellite first observed the thermal X-ray emission from spiral galaxies (Fabbiano 1989), and ROSAT and ASCA subsequently measured the temperature and Fe ISM abundances (Roberts & Warwick 2001; Petre et al. 1994). Chandra and XMM-Newton have enabled us to study the spatial distribution of metals by utilizing their large effective area and high angular resolution (Schlegel et al. 2003; Yang et al. 2007). However, the O and Mg abundance measurements are difficult due to the intrinsic instrumental background and asymmetric energy response in the low energy band below ~ 1 keV. Because Suzaku XIS (Koyama et al. 2007) has higher spectral sensitivity below ~ 1 keV, and a lower and more stable background level compared to Chandra ACIS and XMM-Newton EPIC, the accuracy of the determination of O and Mg abundances is improved. Recent Suzaku observations have revealed the abundance profiles of the ISM in X-ray bright elliptical and starburst galaxies in detail (Matsushita et al. 2007; Tsuru et al. 2007; Tawara et al. 2008; Yamasaki et al. 2009; Hayashi 2009).

NGC 4258 (M 106) is a nearby SABbc spiral galaxy with a high inclination angle of 72° (Tully 1988). Its distance is accurately measured to be 7.2 Mpc (Herrnstein et al. 1999), where $1'$ corresponds to 2.1 kpc. Makishima et al. (1994) first discovered the obscured low-luminosity active galactic nucleus (LLAGN) in NGC 4258 with ASCA, and also showed that its 1–10 keV spectrum is composed of contributions from thermal plasmas, integrated low mass X-ray binaries (LMXBs), and the nucleus. A ROSAT observation detected two thermal components with $kT \sim 0.2$

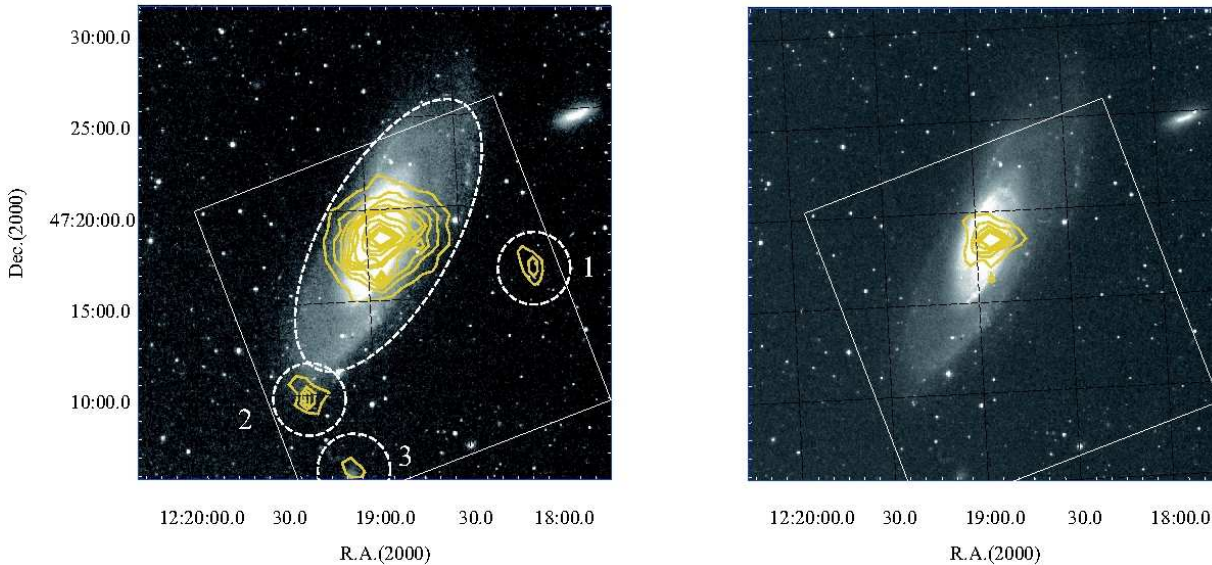


Fig. 1. The X-ray contour map (orange) in linear scale from 0.5–2 keV (left) and 2–10 keV (right), overlaid on an optical image taken by DSS. The contour scales range linear by $(0.17 - 5) \times 10^{-2}$ and $0.3 - 1.3$ counts $\text{sec}^{-1} \text{arcmin}^{-2}$, respectively. The observed XIS0, 1, 2, and 3 images were added on the sky coordinate, and smoothed with $\sigma = 12$ pixel Gaussian profile. Estimated contributions of the cosmic X-ray background (CXB) and the instrumental non X-ray background (NXB) were subtracted, although vignetting was not corrected. The white square corresponds to the field of view of the Suzaku XIS. The region where energy spectra were extracted is indicated by a white dashed ellipse. Three point sources (white dashed circles) were excluded from the background energy spectra.

and ~ 0.5 keV in the ISM (Vogler & Pietsch 1999), which were confirmed with Chandra and XMM-Newton observations (Yang et al. 2007). The 2–10 keV flux from the nucleus was reported to vary on time scales of hours to years (Reynolds et al. 2000; Terashima et al. 2002; Fruscione et al. 2005). A recent Suzaku observation has revealed that the circum-nuclear matter forms a slim obscuring structure with solid angle much smaller than typical thick tori (Yamada et al. 2009; Reynolds et al. 2008). The galaxy has a curious jet-like feature, what is called an “anomalous arms”, emitting soft X-rays (e.g., Cecil et al. 1992, Wilkes et al. 1995; Cecil et al. 1995). In addition, the hot spots associated with the galactic radio jet have been detected at a distance of around $1'$ from the nucleus in X-rays by Chandra (Yang et al. 2007). Aside from these anomalous arms, which seem to be related to the nuclear activity, NGC 4258 can be regarded as being similar to our Galaxy in terms of the low activity of the central black hole. The fact that the emission from the nucleus is deeply absorbed with a thick circum-nuclear matter (Makishima et al. 1994) is helpful to study the thermal emission. In this paper, we report the detailed analysis of NGC 4258 with Suzaku, focusing on the thermal emission of the ISM to constrain the metal abundances.

Unless noted otherwise, the solar abundance table used is taken from given by Anders & Grevesse (1989), and the quoted errors are for a 90% confidence interval for a single interesting parameter.

2. Observation and Data Reduction

Suzaku carried out an observation of NGC 4258 in 2006 June. We analyzed only the XIS data in this paper, although Suzaku observed the object with both XIS and HXD (Takahashi et al. 2007), centered on the HXD field of view, and the HXD results from this observation on the nucleus have already been published by Yamada et al. (2009). The XIS consists of four sets of X-ray CCD camera system (XIS0, 1, 2, and 3). XIS1 has a back-illuminated (BI) sensor, while XIS0, 2, and 3 have front-illuminated (FI) sensors. The averaged pointing direction of the XIS is centered on (R.A., Dec.)= $(12^{\text{h}}18^{\text{m}}50^{\text{s}}.8, +47^{\circ}14'15''.4)$. The XIS was operated in the normal clocking mode (8 s exposure per frame), with the standard 5×5 and 3×3 editing mode. We processed the XIS data by the “xispi” and “makepi” ftools task and the CALDB files of 2008-01-31 version. Then, the XIS data were cleaned by assuming thresholds on the Earth elevation angle of $> 5^{\circ}$ and the Day-earth elevation angle of $> 20^{\circ}$. We also discarded data during the time since the spacecraft exit from the south Atlantic anomaly was less than 436 sec. We created a light curve of each sensor over 0.5–2 keV binned 540 sec to exclude periods of an anomalous event rate greater or less than $\pm 3\sigma$ around the mean. After the above screening, the remaining good exposures were 99.9 and 99.8 ksec for FIs and BI, respectively. Event screening with cut-off rigidity was not performed. We also excluded the RAWY<119 region on the XIS2 and 3 due to an er-

aneous dark frame during this observation.

The spectral analysis was performed with HEASoft version 6.5 and XSPEC 12.4. In order to subtract the non-X-ray background (NXB), we employed the dark-Earth database by the “xisnxbgen” ftools task (Tawa et al. 2008). We generated two different Ancillary Response Files (ARFs) for the spectrum of each region, which assumed uniform sky emission and the observed XIS1 image by the “xissimarfgen” ftools task (Ishisaki et al. 2007). We also included the effect of contaminations on the optical blocking filters of the XIS in the ARFs.

3. Analysis and Results

3.1. Strategy of Spectral Fitting

Figure 1 shows the observed X-ray contours in the 0.5–2 keV and 2–10 keV ranges, overlaid on the optical image from the Digitized Sky Survey (DSS). We extracted spectra from the following two regions.

1. NGC 4258 components: an ellipse region, with semi-major and semiminor axes of 8.3′ and 3.6′.
2. Background: the entire XIS field of view was used, after excluding the above NGC 4258 component and three additional 1.5′ radius circular point source regions mentioned below.

Three X-ray point-like sources were detected in 0.5–2 keV as shown in figure 1. Sources #1, 2, and 3 were identified as a quasar Q 1218+472 (Burbridge 1995), an Ultra Luminous X-ray source (Arp et al. 2004), and an irregular galaxy UGC 7356 (Thuan & Seitzer 1979), respectively. Although these sources were not so bright as to affect the spectra of NGC 4258, these were not negligible with respect to the estimation of the extra-galactic cosmic X-ray background (CXB) and the Galactic emissions. In addition, three calibration sources, which have emission peaks at 5.9 keV, are located at the corners of the XIS. We included these regions for improvement in photon statistics because our target spectra are extracted only over the energy range below 5 keV.

The 0.5–2 keV contours of NGC 4258, which mainly represent the ISM emission, are clearly extended as compared to those in 2–10 keV, which are dominated by the LLAGN emission. Therefore, the soft X-ray signal is considered to arise mainly from an extended hot halo. In fact, Yang et al. (2007) showed that the 0.2–10 keV spectra observed with XMM-Newton were represented by the sum of two thermal components of 0.60 and 0.22 keV, plus the emission from LMXBs and the obscured LLAGN. The resultant parameters of these components imply that, even in the nuclear region within 3′, the diffuse thermal ISM emission dominate the total flux below ~ 2 keV. Thus, we also analyzed the XIS spectra below 2 keV to investigate the ISM properties.

3.2. Estimation of the background spectra

In order to estimate the CXB and Galactic emission background components we first fitted the spectra of the background region. We assumed a power-law model for

the CXB component, and a two temperature model for the Galaxy to represent emission from local hot bubble (LHB) and Milky Way halo (MWH). We tested the following two models: (i) $\text{phabs} \times \text{power-law} + \text{apec}_{\text{MWH}} + \text{apec}_{\text{LHB}}$, and (ii) $\text{phabs} \times (\text{power-law} + \text{apec}_{\text{MWH}}) + \text{apec}_{\text{LHB}}$, where the apec models have a metal abundance fixed at the solar value and zero redshift. The absorption column density was also fixed to the Galactic value in the direction of NGC 4258, which is $1.2 \times 10^{20} \text{ cm}^{-2}$. The difference between the two models is whether the MWH component is absorbed by the Galactic column or not (Yamasaki et al. 2009). We also fixed the temperature of the LHB and MWH emission to be 0.1 and 0.3 keV, respectively, after previous studies (Lumb et al. 2002; Yamasaki et al. 2009; Komiyama et al. 2009). Due to poor photon statistics, leaving either temperature free did not provide useful constraints. The spectra from the BI and FI CCDs were fitted simultaneously in the 0.5–5.0 keV range. The results of these fits are summarized in table 1. The normalization of the power-law model was found to be higher ($\sim 19\%$) than the previously reported value (e.g., Kushino et al. 2002). This may be accounted for as due to the CXB brightness fluctuation, or to possible contamination by point sources in NGC 4258. Although the results do not differ significantly between the two models, model (ii) gave a marginally better fit statistic, $\chi^2/\text{d.o.f.} = 558/426$.

In order to estimate the Galactic emission, we fitted the OVII and OVIII lines with Gaussian and a power-law in the 0.5–0.7 keV range. The resultant intensities of the OVII and OVIII without correcting for absorption are 3.8 ± 1.1 and 1.1 ± 0.9 photons $\text{cm}^{-2} \text{ s}^{-1} \text{ sr}^{-1}$, respectively. These are consistent with previously reported values (McCammon et al. 2002; Sato et al. 2007; Yamasaki et al. 2009). Hereafter, model (ii) is utilized as the background for the spectral fitting, unless otherwise stated.

3.3. The galaxy spectra of NGC 4258

We fitted the galaxy spectra with the model: $\text{phabs}_{\text{G}} \times (\text{vapec}_{1\text{T},2\text{T},\text{or}3\text{T}} + \text{bremss}) + \text{phabs}_{\text{AGN}} \times \text{power-law}_{\text{AGN}} + \text{phabs}_{\text{G}} \times (\text{power-law}_{\text{CXB}} + \text{apec}_{\text{MWH}}) + \text{apec}_{\text{LHB}}$, where the last term represents the background model to be explained later. In the model, phabs_{G} means the Galactic absorption in the direction of NGC 4258, fixed at $N_{\text{H}} = 1.2 \times 10^{20} \text{ cm}^{-2}$. The term ($\text{phabs}_{\text{AGN}} \times \text{power-law}_{\text{AGN}}$) shows the LLAGN contribution; its absorbing column was fixed at $1.07 \times 10^{20} \text{ cm}^{-2}$, and the $\text{power-law}_{\text{AGN}}$ slope and normalization at $\Gamma = 1.86$ and $\text{Norm} = 4.22 \times 10^{-3}$ photons $\text{keV}^{-1} \text{ cm}^{-2} \text{ s}^{-1}$ at 1 keV, both after Yamada et al. (2009). This formalism assumes that the absorption within NGC 4258 follows the same abundance ratios as the Galactic ones employed in the phabs model. This assumption is justified *a posteriori* by our result to be obtained below, that NGC 4258 and our Galaxy have rather similar abundance patterns. Although the intensity of the LLAGN component is much lower than that of the ISM components below 2 keV (subsection 3.1), we take this term into account to decide accurately the emission of the Si-K α line around 1.8 keV where the LLAGN emission may affect the spectral fits. The term

Table 1. The best-fit parameters of the apec component + power-law model.*

Parameters	(i)	(ii)
Γ_{CXB}	1.38 ± 0.05	1.37 ± 0.05
$Norm_{\text{CXB}}^\dagger$	$1.16^{+0.05}_{-0.06}$	$1.15^{+0.05}_{-0.06}$
N_{H} (cm ⁻²)	1.2×10^{20} (fix)	1.2×10^{20} (fix)
kT_{MWH} (keV)	0.3 (fix)	0.3 (fix)
Abundance (solar)	1 (fix)	1 (fix)
$Norm_{\text{MWH}}^\ddagger$	0.64 ± 0.06	0.68 ± 0.06
kT_{LHB} (keV)	0.1 (fix)	0.1 (fix)
Abundance (solar)	1 (fix)	1 (fix)
$Norm_{\text{LHB}}^\dagger$	$1.74^{+0.36}_{-0.37}$	$1.80^{+0.36}_{-0.37}$
$\chi^2/\text{d.o.f.}$	562/426	558/426

* The apec components for the spectra in the background region of NGC 4258 with absorbed or non-absorbed MWH component for the Galactic emission, and a power-law model for CXB.

[†] Normalization of the power-law component divided by the solid angle, Ω^u , assumed in the uniform-sky ARF calculation (20' radius), in units of $10^{-3} \Omega^u$ photons keV⁻¹ cm⁻² s⁻¹ arcmin⁻² at 1 keV.

[‡] Normalization of the apec components divided by the solid angle same as the normalization of apec, $Norm = \int n_e n_H dV / (4\pi (1+z)^2 D_A^2) / \Omega^u \times 10^{-17}$ cm⁻⁵ arcmin⁻², where D_A is the angular distance to the source.

($\text{phabs}_G \times (\text{power-law}_{\text{CXB}} + \text{apec}_{\text{MWH}}) + \text{apec}_{\text{LHB}}$) represents the background component as examined in subsection 3.2.

The ISM emission of NGC 4258 was modeled with one, two, or three-temperature models, as indicated by the subscripts 1T, 2T, or 3T, respectively, employing the vepc code (Smith et al. 2001). The abundances of He, C, and N were fixed to the solar value. We also divided the other metals into five groups as O, Ne, (Mg & Al), (Si, S, Ar, Ca), and (Fe & Ni), based on the metal synthesis mechanism of SNe, and allowed them to vary. The abundances were constrained to be common all temperature components. The brems model, with $kT = 10$ keV, represents the integrated LMXB component (Makishima et al. 1994; Yamada et al. 2009). In order to constrain the background component contained in the above fitting model, we simultaneously fitted the source and background spectra, over the 0.5–2 keV and 0.5–5 keV regions, respectively. When fitting the background spectra, the normalizations of vepc, brems, and power-law_{AGN} were all fixed to be 0.

The results of these fits are shown in figure 2, and the derived parameters are summarized in table 2. Thus, several emission lines are seen around 0.5–0.6 keV, 0.6–0.7 keV, ~ 1.3 keV, and ~ 1.8 keV, and are identified with those of O VII, O VIII, Mg XI and Si XIII, respectively. Furthermore, emission lines around 0.7–1 keV correspond to the Fe-L complex, as well as to K-lines from Ne IX and Ne X. The fits are not formally acceptable because of the big residuals around 2 keV owing to calibration issues of Si edges, which are known to be present in all the XIS CCDs (Koyama et al. 2007). However, these results are still useful to assess whether the temperatures and metal abundances in the ISM were reasonably determined or not. The one-temperature model results in $kT = 0.38$ keV. The fit statistics shown in table 2 clearly favor the two-

temperature model, which gives the two temperatures as 0.23 and 0.59 keV, with corresponding 0.2–2.4 keV unabsorbed fluxes of 1.0×10^{-12} and 2.5×10^{-12} erg cm⁻² s⁻¹, respectively. The 0.1–2.4 keV total unabsorbed ISM luminosity is 2.2×10^{40} erg s⁻¹, which is consistent with that of the previous XMM-Newton results (Yang et al. 2007). The three-temperature model improved the fit statistics only slightly, and yielded the temperatures as 0.13, 0.36, and 0.62 keV. The implied abundance ratios did not change, as shown in table 2.

In order to examine abundance ratios rather than absolute values, we calculated confidence contours between the abundance of metals (O, Ne, Mg and Si) and that of Fe, using the two-temperature model for the ISM. The results are shown in figure 3, where we also indicate 90%-confidence abundance of these metals relative to Fe.

3.4. Systematic Uncertainties in the Abundance Ratios

In order to investigate how these results are sensitive to the assumed Galactic model, we let the temperatures of the MWH and LHB vary freely. Although the temperatures of the Galactic components became 0.17 and 0.61 keV, the ISM abundance ratios were little affected. When we change the normalizations of Galactic apec_{MWH} and apec_{LHB} by $\pm 10\%$ and $\pm 20\%$, respectively, the metals to Fe abundance ratios of the ISM remained the same within $\sim 5\%$. The systematic uncertainty due to the assumption of the OBF contaminant is less than the statistical error in the NGC 4258 region. Thus, the uncertainties in the background and the OBF contaminant have little effect on the abundance ratios of the NGC 4258 ISM.

Next, we investigate uncertainties in the absorption parameter. Although we have carried out the fits with the absorption fixed to the Galactic value, Yang et al. (2007) have shown that absorption varies by a factor of a few, depending on location. When we fit the spectra with the

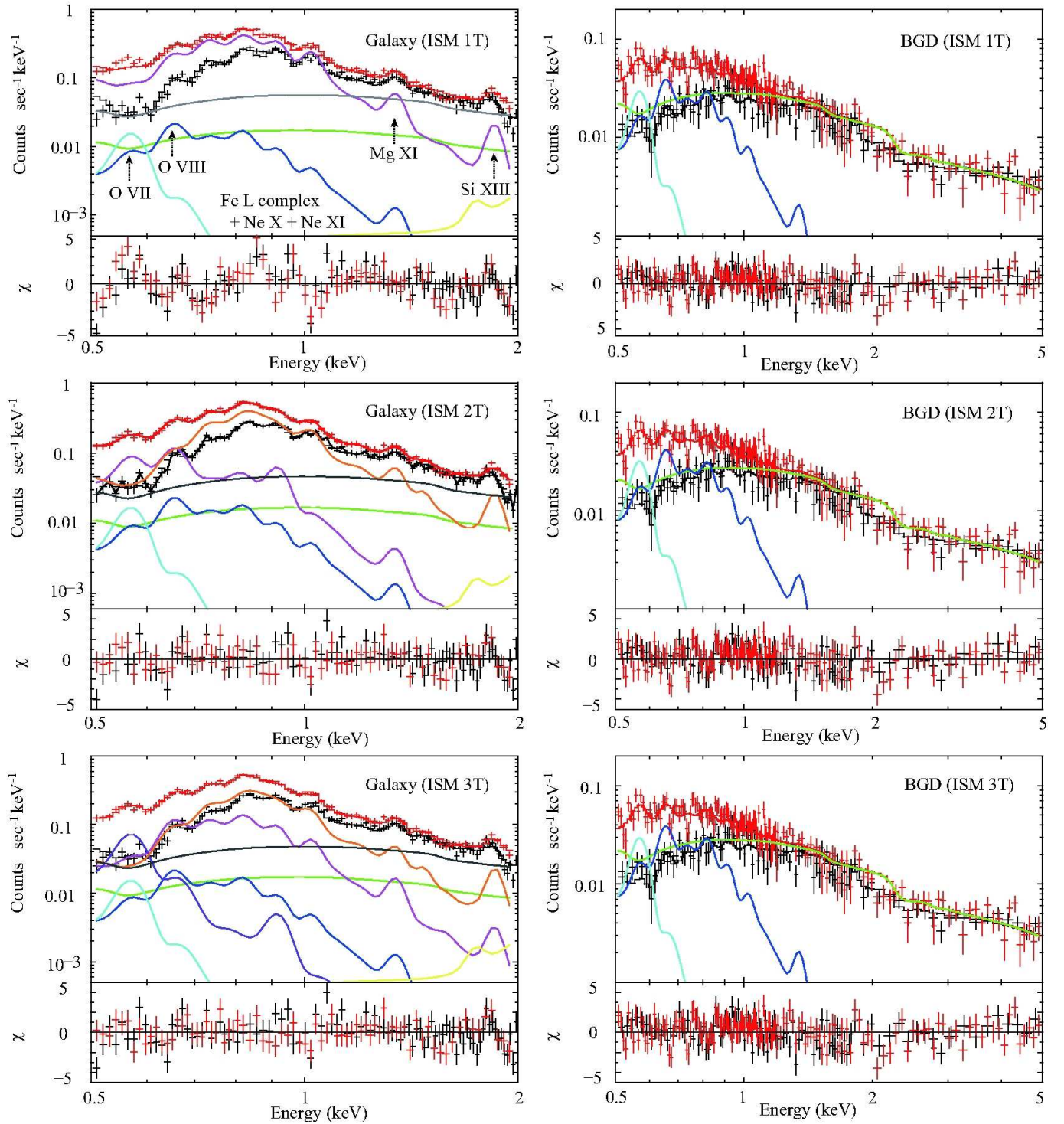


Fig. 2. The NXB-subtracted XIS-FI (black) and XIS-BI (red) spectra of NGC 4258 (left column), and those of the background region, shown without removing the instrumental responses. Each spectrum from the top to bottom panel was fitted with a one, two, or three-temperature model for the ISM, respectively. The black and red lines show the best-fit model for the FI and BI, respectively. For simplicity, only the model components for BI spectra are shown. The magenta, orange, and purple lines are the ISM components, blue and cyan are the Galactic background emission by apec_{MWH} and apec_{LHB} , and green, gray, and yellow are the CXB, LMXB, and LLAGN components, respectively. The background components are common between the on-source and background spectra.

Table 2. Summary of the best-fit parameters of the NGC 4258 and background region.

Parameters	1T for ISM	2T for ISM	2T for ISM (LHB and MWH free)	3T for ISM
Γ_{CXB}	1.42	1.41±0.04	1.31 ^{+0.04} _{-0.06}	1.41±0.04
$Norm_{\text{CXB}}^*$	1.21	1.21±0.04	1.08 ^{+0.03} _{-0.02}	1.21±0.04
kT_{MWH} (keV)	0.3 (fix)	0.3 (fix)	0.61 ^{+0.57} _{-0.03}	0.3 (fix)
$Norm_{\text{MWH}}^\dagger$	0.68 (fix)	0.68 (fix)	0.32 ^{+0.03} _{-0.04}	0.68 (fix)
kT_{LHB} (keV)	0.1 (fix)	0.1 (fix)	0.17±0.01	0.1 (fix)
$Norm_{\text{LHB}}^\dagger$	1.80 (fix)	1.80 (fix)	0.88 ^{+0.07} _{-0.08}	1.80 (fix)
$kT_{1\text{T}}$ (keV)	0.38±0.01	0.23±0.01	0.24±0.01	0.13 ^{+0.36} _{-0.06}
$Norm_{1\text{T}}^\dagger$	2.18±0.04	0.68 ^{+0.15} _{-0.19}	0.72 ^{+0.04} _{-0.05}	0.41 ^{+0.11} _{-0.02}
$kT_{2\text{T}}$ (keV)	-	0.56±0.01	0.58±0.01	0.36 ^{+0.06} _{-0.05}
$Norm_{2\text{T}}^\dagger$	-	1.15 ^{+0.06} _{-0.42}	1.27 ^{+0.26} _{-0.03}	0.52 ^{+0.03} _{-0.02}
$kT_{3\text{T}}$ (keV)	-	-	-	0.62 ^{+0.06} _{-0.02}
$Norm_{3\text{T}}^\dagger$	-	-	-	0.68 ^{+0.04} _{-0.02}
O (solar)	0.36 ^{+0.10} _{-0.07}	0.56 ^{+0.17} _{-0.08}	0.53 ^{+0.03} _{-0.04}	0.91 ^{+0.24} _{-0.32}
Ne (solar)	1.20 ^{+0.29} _{-0.20}	1.28 ^{+0.62} _{-0.20}	1.12 ^{+0.06} _{-0.07}	1.43 ^{+0.51} _{-0.46}
Mg, Al (solar)	0.79 ^{+0.21} _{-0.15}	0.99 ^{+0.47} _{-0.15}	0.87 ^{+0.13} _{-0.11}	1.25 ^{+0.42} _{-0.41}
Si,S,Ar,Ca (solar)	1.59 ^{+0.54} _{-0.39}	1.11 ^{+0.50} _{-0.18}	0.99 ^{+0.13} _{-0.11}	1.42 ^{+0.47} _{-0.45}
Fe, Ni (solar)	0.49 ^{+0.12} _{-0.08}	0.64 ^{+0.29} _{-0.09}	0.57 ^{+0.01} _{-0.02}	0.84 ^{+0.20} _{-0.27}
LMXB flux [‡] (erg cm ⁻² s ⁻¹)	9.2 × 10 ⁻¹³	7.9 × 10 ⁻¹³	7.7 × 10 ⁻¹³	7.8 × 10 ⁻¹³
$\chi^2/\text{d.o.f.}$	1333/740	993/738	946/734	982/736

* Normalization of the power-law component divided by the solid angle, Ω^v , assumed in the uniform-sky ARF calculation (20' radius), in units of $10^{-3} \Omega^v$ photons keV⁻¹ cm⁻² s⁻¹ arcmin⁻² at 1 keV.

† Normalization of the vaped component scaled with a factor of $\text{SOURCE_RATIO_REG} / \text{AREA}$, which is $Norm = \frac{\text{SOURCE_RATIO_REG}}{\text{AREA}} \int n_e n_H dV / [4\pi(1+z)^2 D_A^2] \times 10^{-17} \text{ cm}^{-5} \text{ arcmin}^{-2}$, where D_A is the angular distance to the source.

‡ Flux within the accumulated region between 0.5 and 2 keV.

absorption allowed to vary freely, the resultant absorption is constrained with an upper limit of N_{H} of $4.7 \times 10^{20} \text{ cm}^{-2}$. Thus, we confirm that the effect of the absorption is almost negligible because the resultant abundance change insignificantly.

In order to examine the dependence on the LMXB component, we used power-law model instead of the brems model in Makishima et al. (1994) and Yamada et al. (2009). However, the abundance ratios to Fe did not change significantly either.

The derived Ne to Fe abundance ratio is higher by a factor of ~ 2 higher than the solar abundance. This is presumably because the Ne abundance is not reliably determined due to an overlap with the strong and complex Fe-L line emissions.

Yang et al. (2007) have detected the hot spots of the jet located around 1' from the nucleus in X-rays, and also found a non-thermal component besides that from the AGN within a 20'' region centered on the nucleus. In order to examine the contribution of the jet emission, we tried to investigate the spatial distribution of the metal abundances. Because the above physical scales are much smaller than the nominal 3' point spread function of Suzaku (Serlemitsos et al. 2007), we are only able to place crude constraints. We first extracted spectra from two

separate regions for comparison: (i) a circular aperture of radius 3' centered on the nucleus, and (ii) the remainder of the elliptical data-accumulation region from figure 1, excluding the central 3'. We fitted the two spectra with the two-temperature model. Unfortunately, poor photon statistics prevented the detection of any significant abundance differences between the two regions. Thus we carried out a different test in which we added the following jet model from Yang et al. (2007) to the two-temperature model : $\text{phabs}_{\text{jet}} \times \text{power-law}_{\text{jet}}$. Here, $\text{phabs}_{\text{jet}}$, the intrinsic absorption, was fixed at $3.4 \times 10^{21} \text{ cm}^{-2}$, and the photon index of $\text{power-law}_{\text{jet}}$ was fixed at 1.74 (Yang et al. 2007). Then, the 0.5–2 keV jet emission flux was rather tightly constrained to be $< 4.5 \times 10^{-14} \text{ erg cm}^{-2} \text{ s}^{-1}$, at a confidence limit of 90%. Because the other parameters, including the metal abundances, did not change significantly, we conclude that our results are not affected by the jet emission.

4. Discussion

The present Suzaku observation has clearly revealed emission line features from the ISM in the spiral galaxy NGC 4258. We successfully measured the metal abundances of O, Ne, Mg, Si and Fe for the first time. Previous

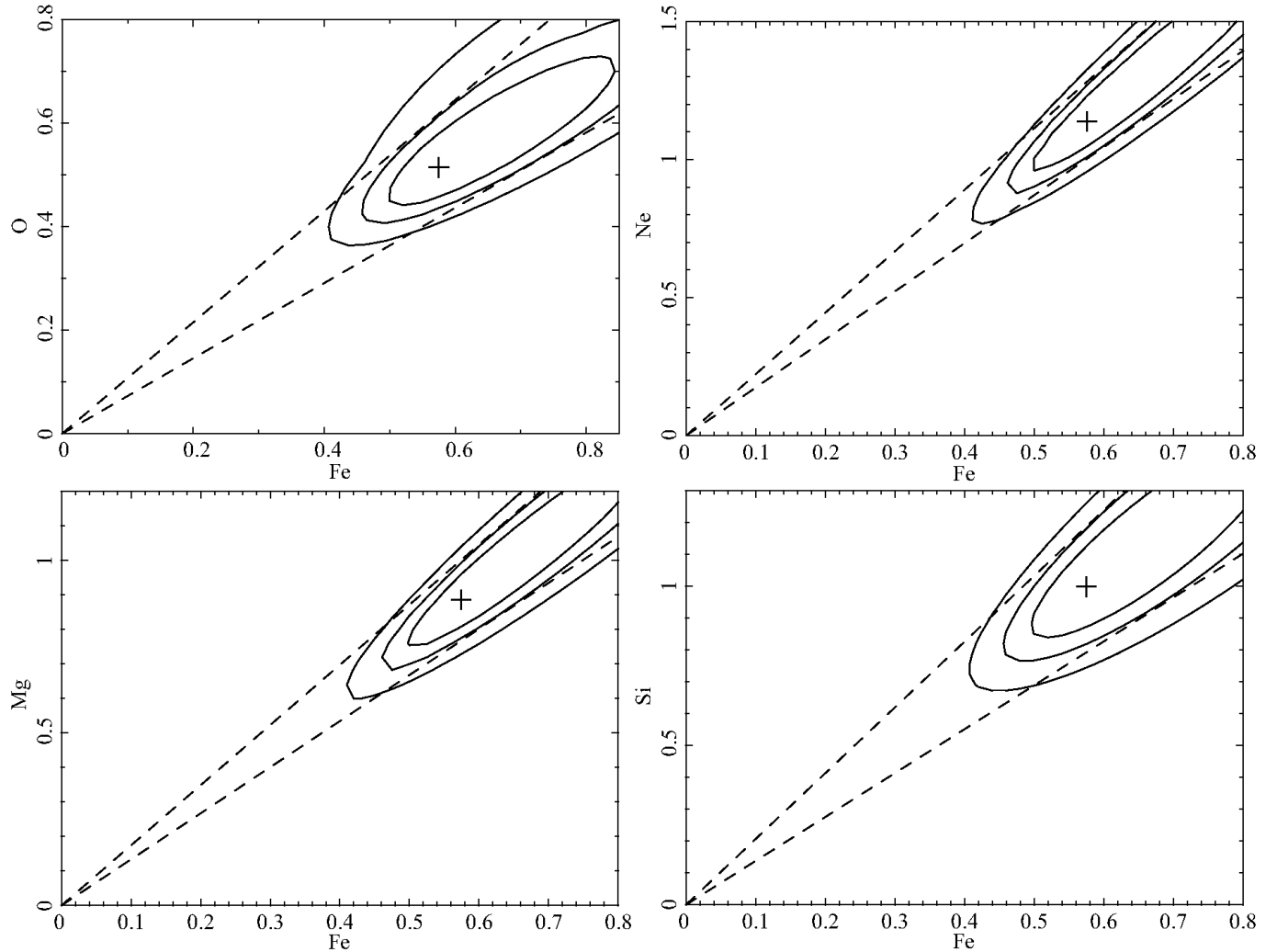


Fig. 3. Plot of the confidence contours between the metal (O, Mg, S, Si) and Fe abundances, indicated by the two-temperature model for the ISM. The three contours represent 68%, 90%, and 99% confidence range from inner to outer, respectively.

observations with XMM-Newton and Chandra with better angular resolutions successfully measured spatial temperature variations and the geometric structure of “anomalous arms”. But, the metal abundances were not constrained due to insufficient photon statistics (Yang et al. 2007). Figure 4 shows our metal-to-Fe ratios, which were derived from the two-parameter confidence contours in figure 3. The ISM emission is here modeled with two temperatures.

In figure 4, the abundance pattern of NGC 4258 is compared with those indicated by the solar abundance table of Anders & Grevesse (1989) and the new solar abundance table of Lodders (2003). The O abundance in Lodders (2003) was derived from solar photospheric lines, considering three-dimensional hydrostatic model atmospheres and non-local thermodynamic equilibrium (Asplund 2005 and references therein). Thus, the abundance pattern of the ISM of NGC 4258 measured with Suzaku agrees better with that of Lodders (2003), rather than that of Anders & Grevesse (1989).

The calculated SN II and SN Ia yields are also plotted

in figure 4. Here, the SN II yields by Nomoto et al. (2006) refer to an average over the Salpeter initial mass function of stellar masses from 10 to 50 M_{\odot} , with a progenitor metallicity of $Z = 0.02$. The SN Ia yields were taken from the W7 model Iwamoto et al. (1999). The abundance pattern of the ISM of NGC 4258 is located between those of SN II and SN Ia, and consistent with their mixture is.

In order to investigate differences between spiral and starburst galaxies, we also plot in figure 4 the abundance pattern of the hot ISM in disk and halo regions of the starburst galaxy NGC 4631 (Yamasaki et al. 2009), and that of the “cap” region of the extreme starburst galaxy M 82 (Tsuru et al. 2007). The results of NGC 4631 disk are consistent with those of Lodders (2003) as is the case of NGC 4258, while the respective patterns of M 82 “cap” and the halo region of NGC 4631 are close to those expected from SN II yields.

The SFR of NGC 4258 derived from its far infrared luminosity is low, $\sim 0.01 M_{\odot} \text{ yr}^{-1}$ (Wu & Cao 2006), compared with those of NGC 4631 and M 82, which are 2.99 and 9.39 $M_{\odot} \text{ yr}^{-1}$, respectively (Tüllmann et al. 2006).

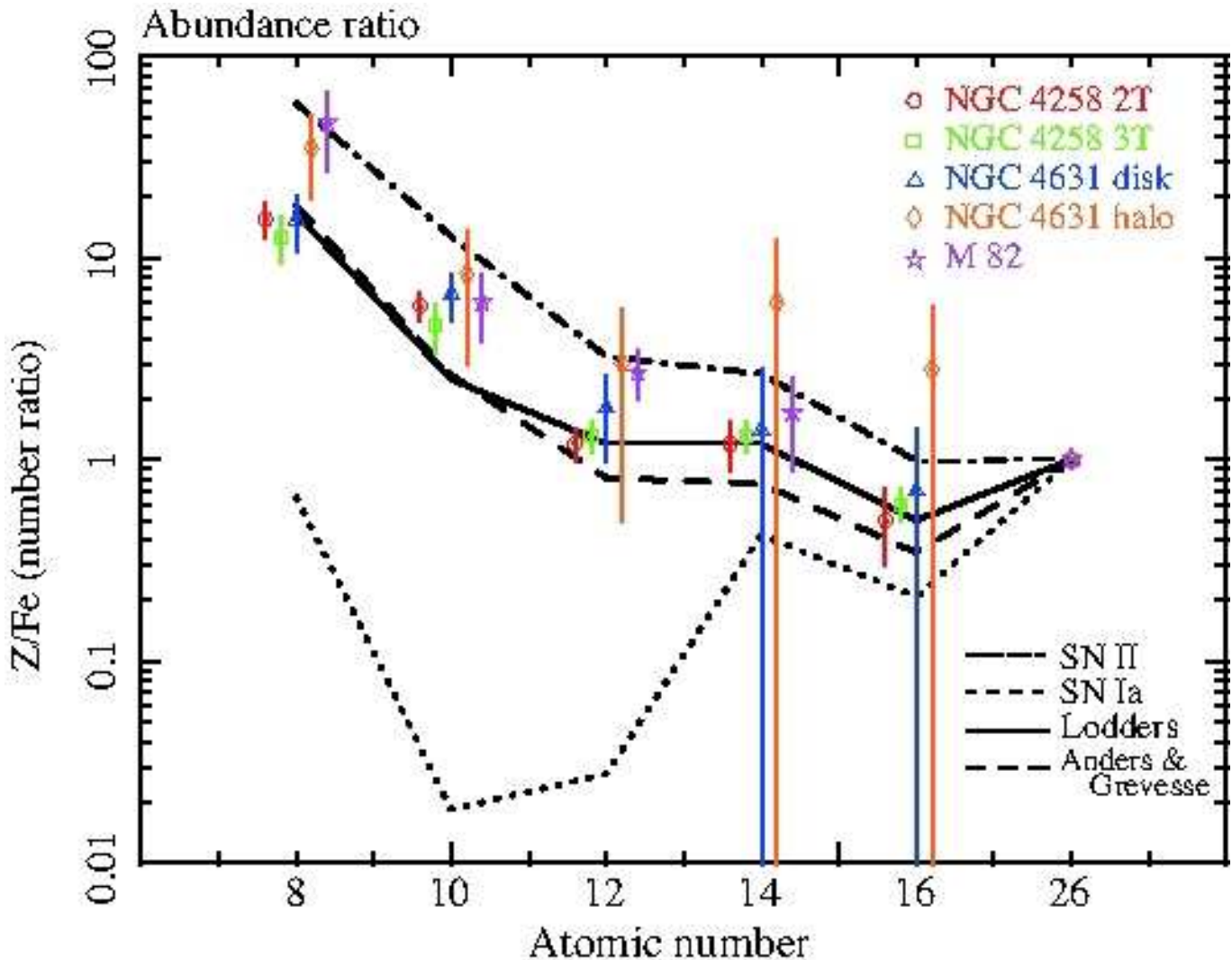


Fig. 4. Number ratios of O, Ne, Mg, Si and S to Fe for the two and three-temperature model of the ISM in NGC 4258. Solid and dashed lines indicate the number ratios of metals to Fe due to Lodders (2003) and Anders & Grevesse (1989), respectively. Abundance patterns of NGC 4631 disk, halo (Yamasaki et al. 2009), and M 82 “cap” (Tsuru et al. 2007) also are shown. Dot-Dashed and dotted lines represent the number ratios of metals to Fe for the SN II and SN Ia products (Iwamoto et al. 1999; Nomoto et al. 2006).

The 0.5–2 keV luminosity of the LMXB component of NGC 4258, 3.5×10^{39} erg s⁻¹, is consistent with the mass vs. X-ray luminosity relation for spiral galaxies (Gilfanov 2004). Thus, we can regard NGC 4258 as a “normal” spiral galaxy. Therefore, we may conclude that solar abundance patterns are common in normal spiral galaxies, including NGC 4258 and our Galaxy. The fact that the disk region of NGC 4631 also has a similar abundance pattern to normal spirals, suggests that the metallicity of the ISM after its starburst era may look quite similar. In contrast, in starburst galaxies, SN II products such as O effectively escape into the halo region as a result of the energetic explosions. Thus, observations of abundance patterns such as ours play a key role in investigating the processes of galaxy evolution and enrichment of the intergalactic medium.

We thank the referee for providing valuable comments. We gratefully acknowledge all members of the Suzaku hardware and software teams and the Science Working Group. KS acknowledges support by the Ministry of Education, Culture, Sports, Science and Technology of Japan, Grant-in-Aid for Scientific Research No. 21740134. PG acknowledges a RIKEN Foreign Postdoctoral Research Fellowship.

References

- Anders, E., & Grevesse, N. 1989, *Geochim. Cosmochim. Acta*, 53, 197
- Asplund, M. 2005, *ARA&A*, 43, 481
- Arp, H., Gutiérrez, C. M., & López-Corrodoira, M. 2004, *A&A*, 418, 877
- Burbidge, E. M. 1995, *A&A*, 298, L1
- Cecil, G., Morse, J. A., & Veilleux, S. 1995, *ApJ*, 452, 613

- Cecil, G., Wilson, A. S., & Tully, R. B. 1992, *ApJ*, 390, 365
- Crockett, N. R., Garnett, D. R., Massey, P., & Jacoby, G. 2006, *ApJ*, 637, 741
- Fabbiano, G. 1989, *ARA&A*, 27, 87
- Fruscione, A., Greenhill, L. J., Filippenko, A. V., Moran, J. M., Herrnstein, J. R., & Galle, E. 2005, *ApJ*, 624, 103
- Gilfanov, M. 2004, *MNRAS*, 349, 146
- Hayashi, T. et al. 2009 submitted to *PASJ*
- Herrnstein, J. R., et al. 1999, *Nature*, 400, 539
- Ishisaki, Y., et al. 2007, *PASJ*, 59, 113
- Iwamoto, K., Brachwitz, F., Nomoto, K., Kishimoto, N., Umeda, H., Hix, W. R., & Thielemann, F.-K. 1999, *ApJS*, 125, 439
- Komiyama, M., Sato, K., Nagino, R., Ohashi, T., & Matsushita, K. 2009, *PASJ*, 61, 337
- Koyama, K., et al. 2007, *PASJ*, 59, 23
- Kushino, A., Ishisaki, Y., Morita, U., Yamasaki, N. Y., Ishida, M., Ohashi, T., & Ueda, Y. 2002, *PASJ*, 54, 327
- Lodders, K. 2003, *ApJ*, 591, 1220
- Lumb, D. H., Warwick, R. S., Page, M., & De Luca, A. 2002, *A&A*, 389, 93
- Makishima, K., et al. 1994, *PASJ*, 46, L77
- Matsushita, K., et al. 2007, *PASJ*, 59, 327
- McCammon, D., et al. 2002, *ApJ*, 576, 188
- Nomoto, K., Tominaga, N., Umeda, H., Kobayashi, C., & Maeda, K. 2006, *Nuclear Physics A*, 777, 424
- Ozawa, M., et al. 2009, *PASJ*, 61, 1
- Pérez-Montero, E., Hägele, G. F., Contini, T., & Díaz, Á. I. 2007, *MNRAS*, 381, 125
- Petre, R., Okada, K., Mihara, T., Makishima, K., Schlegel, E., & Colbert, E. 1994, *Bulletin of the American Astronomical Society*, 26, 940
- Reynolds, C. S., Nowak, M. A., & Maloney, P. R. 2000, *ApJ*, 540, 143
- C. Reynolds, Nowak, M. A., Markoff, S., Tueller, J., Wilms, J., Young, A. J., 2008, *ApJ*, 691, 1159
- Roberts, T. P., & Warwick, R. S. 2001, *X-ray Astronomy:Stellar Endpoints, AGN, and the Diffuse X-ray Background*, 599, 474
- Sato, K., Tokoi, K., Matsushita, K., Ishisaki, Y., Yamasaki, N. Y., Ishida, M., & Ohashi, T. 2007, *ApJL*, 667, L41
- Sato, K., et al. 2007, *PASJ*, 59, 299
- Schlegel, E. M., Holt, S. S., & Petre, R. 2003, *ApJ*, 598, 982
- Serlemitsos, P. J., et al. 2007, *PASJ*, 59, 9
- Smith, R. K., Brickhouse, N. S., Liedahl, D. A., & Raymond, J. C. 2001, *ApJL*, 556, L91
- Takahashi, T., et al. 2007, *PASJ*, 59, 35
- Tawa, N., et al. 2008, *PASJ*, 60, 11
- Tawara, Y., Matsumoto, C., Tozuka, M., Fukazawa, Y., Matsushita, K., & Anabuki, N. 2008, *PASJ*, 60, 307
- Terashima, Y., Iyomoto, N., Ho, L. C., & Ptak, A. F. 2002, *ApJS*, 139, 1
- Thuan, T. X., & Seitzer, P. O. 1979, *ApJ*, 231, 327
- Tsuru, T. G., et al. 2007, *PASJ*, 59, 269
- Tüllmann, R., Breitschwerdt, D., Rossa, J., Pietsch, W., & Dettmar, R.-J. 2006, *A&A*, 457, 779
- Tully, R. B. 1988, *Science*, 242, 310
- Wu, Q., & Cao, X. 2006, *PASP*, 118, 1098
- Vogler, A., & Pietsch, W. 1999, *A&A*, 352, 64
- Wilkes, B. J., Schmidt, G. D., Smith, P. S., Mathur, S., & McLeod, K. K. 1995, *ApJL*, 455, L13
- Yamada, S., Itoh, T., Makishima, K., & Nakazawa, K. 2009, *PASJ*, 61
- Yamasaki, N. Y., Sato, K., Mitsuishi, I., & Ohashi, T. 2009, *PASJ*, 61, 291
- Yang, Y., Li, B., Wilson, A. S., & Reynolds, C. S. 2007, *ApJ*, 660, 1106